

# Tailoring $\gamma$ -austenite Stability to Improve Strength and Toughness of a Medium-Mn Steel



D.M. FIELD, D.J. MAGAGNOSC, B. C HORNBUCKLE, J.T. LLOYD,  
and K.R. LIMMER

A medium-Mn steel with nominal composition 0.20C–5Mn–0.2Si–0.2Al–bal.Fe (in wt pct) was hot rolled to plate and heat-treated at temperatures ranging from 550 °C to 650 °C and times ranging from 1 to 20 hours to obtain different  $\gamma$ -austenite fractions and stabilities, with the remainder of the microstructure being a combination of either  $\alpha$ -ferrite or  $\alpha$ -ferrite +  $\theta$ -carbides. It was shown that when the steel was heat-treated to produce greater quantities of room temperature metastable  $\gamma$ -austenite, the  $\gamma$ -austenite was less stable as the austenite-stabilizing elements were dispersed among a greater fraction of material. Austenite stability, which is correlated with the  $M_s^z$  temperature, was calculated thermodynamically by measuring the local phase composition *via* Atom Probe Tomography. Quasi-static tension and Charpy V-notch (CVN) testing revealed that the austenite stability is directly correlated with CVN energy, where more stable austenite produces increased values of CVN toughness from room temperature down to – 80 °C. We observed that reduced CVN toughness at – 80 °C and – 40 °C in materials with low austenite stability was due to  $\gamma$ -austenite transformation during cooling prior to CVN testing. This work highlights that for materials with high strength and CVN toughness, it is critical to pursue heat treatments that balance both the concentration and stability of  $\gamma$ -austenite, instead of concentration alone. This work further demonstrates the importance of nano-scale composition in the  $\gamma$ -austenite and the utility of fine  $\theta$ -carbide particles in producing steels with moderate strength and superior low temperature toughness.

<https://doi.org/10.1007/s11661-022-06683-5>

This is a U.S. government work and not under copyright protection in the U.S.; foreign copyright protection may apply 2022

## I. INTRODUCTION

MEDIUM-MN transformation and twinning induced plasticity (TRIP and TWIP) steels are originally based on the 0.1C–5Mn (in wt pct) systems from the work of Miller.<sup>[1]</sup> Intercritical annealing (ICA) within the  $\gamma$ -austenite +  $\alpha$ -ferrite phase field<sup>[2–16]</sup> was required to stabilize the  $\gamma$ -austenite down to room temperature through the partitioning of elements like Mn and C to create thermally stable  $\gamma$ -austenite. To achieve this effect it has been shown that extended (>1 hour) heat treatments are required to produce  $\gamma$ -austenite at room temperature and obtain the targeted properties. Properties of these alloys have been reported with ultimate tensile strengths as high as 1548 MPa and total

elongation of 15 pct.<sup>[17]</sup> Typical temperatures for these ICA processes are 550 °C to 680 °C due to the balance between kinetics for elemental partitioning and the thermodynamics for  $\gamma$ -austenite stabilization. Stabilization of the  $\gamma$ -austenite is achieved through the diffusion of elements, such as manganese, nickel, carbon, and nitrogen, which are highly effective<sup>[1,5,11,18–20]</sup> at thermally stabilizing  $\gamma$ -austenite down to room temperature. Nickel-containing steels are also an avenue for producing high toughness alloys for cryogenic (– 197 °C) applications and operate on the principal of producing Ni-enriched  $\gamma$ -austenite that is thermally stable down to the target application temperature.<sup>[19,20]</sup>

It should be noted that most investigations have been limited to primarily thin sheet steels ( $\leq 1.5$  mm). Sheet product processing conventionally involves hot-rolling followed by cold rolling with the application of a post-cold rolling heat treatment. The high reduction ratios provide faster kinetics due to reduced diffusional distances, higher dislocation densities, and greater levels of homogeneity. Consequently, the thinner gauges means that the CVN energy is rarely measured, and the reported toughness is the product of the ultimate strength and ductility as measured by quasi-static

D. M. FIELD, D. J. MAGAGNOSC, B. C HORNBUCKLE, J. T. LLOYD, and K. R. LIMMER are with the Weapons and Materials Research Directorate, U.S. Army Combat Capabilities Development Command Army Research Laboratory, Aberdeen Proving Ground 21005. Contact e-mail: daniel.m.field6.civ@army.mil.

Manuscript submitted December 30, 2021; accepted April 5, 2022.

Article published online April 25, 2022

tension tests. For plate steels, as opposed to sheet, it has been well documented that there are at least two means to improve the low temperature toughness of high strength steels: grain refinement<sup>[21,22]</sup> and thermally stabilized  $\gamma$ -austenite through heat treatment.<sup>[17–19]</sup> In such steels, the  $\gamma$ -austenite must be both thermally and mechanically stable to prevent transformation of fresh, brittle martensite during either cooling to the test temperature or impacting the material. Hu *et al.*<sup>[19]</sup> noted that in a 0.45C–0.25Si–5.6Mn–0.25Cu–0.3Ni–0.2Mo–bal.Fe (wt pct) steel for certain ICA temperatures the  $\gamma$ -austenite was not sufficiently thermally stable and would transform to  $\alpha$ -martensite upon cooling before impact testing at  $-40\text{ }^\circ\text{C}$  and  $-80\text{ }^\circ\text{C}$ . Chen *et al.*<sup>[23]</sup> and Holloman and Jaffe<sup>[24]</sup> also demonstrated that the  $\gamma$ -austenite will transform to fresh martensite during testing which results in brittle fracture thereby reducing the absorbed energy during impact. The global composition of the alloy and the stable phases (*i.e.* carbides or nitrides) can denude the  $\gamma$ -austenite of critical stabilizing elements like Ni, Mn, N or C and exacerbate the instability of the  $\gamma$ -austenite. The work of Niikura and Morris<sup>[18]</sup> found that while a greater volume of  $\gamma$ -austenite could be obtained with increased Mn up to 8 wt pct, as corroborated in the work of Kim *et al.*,<sup>[4]</sup> the toughness was significantly degraded as compared to the base alloy, 0.04C–5Mn–0.2Mo–bal.Fe (in wt pct). Their work noted that the reduction in toughness of the 8Mn alloy was due to the ingress of  $\varepsilon$ -martensite during testing. Niikura and Morris<sup>[18]</sup> expected an increase in toughness as tempering time was increased leading to a subsequent yield strength decrease; however due to the appearance of  $\varepsilon$ -martensite (up to 30 vol pct) the fracture area transition temperature (FATT) shifted up by  $100\text{ }^\circ\text{C}$  to  $125\text{ }^\circ\text{C}$  depending upon the tempering time and  $\varepsilon$ -martensite content; with higher  $\varepsilon$ -martensite contents leading to a greater shift. This shows that  $\varepsilon$ -martensite lead to an increase in the transition temperature from ductile to brittle fracture behavior. However, they also showed that the 8Mn exhibited a higher degree of work-hardening with a yield to ultimate tensile strength ratio of  $\sim 0.63$ . To obtain these properties Niikura and Morris utilized a cyclic heat treatment to refine the  $\alpha$ -martensite packet size from 10 to 20  $\mu\text{m}$  in the quenched and tempered condition to a 3 to 8  $\mu\text{m}$  packet size after a double austenitize-ICA cycle. This heat treatment reduced the DBTT to below cryogenic temperatures ( $-197\text{ }^\circ\text{C}$ ). The increase in low temperature toughness was attributed to the precipitation of fresh  $\gamma$ -austenite at the prior-austenite grain boundaries (PAGBS).

The precipitation of  $\gamma$ -austenite is not the only potential product phase during intercritical annealing. The yield strengths of medium-Mn steels in the hot-rolled condition are very low ranging from 200 to 600 MPa depending upon the processing.<sup>[2–18,25]</sup> To improve the yield strength alloys have been designed with carbide forming elements (Mo, Nb, V, and Cr) to precipitate carbides and improve strength after heat treatment. It was noted in these works that these carbides are beneficial for increasing the strength, however they can reduce the stability of the precipitated

$\gamma$ -austenite by tying up carbon, the most powerful  $\gamma$ -austenite stabilizing element. It is therefore imperative for the alloy designer to consider the ability to produce sufficiently stable  $\gamma$ -austenite within steels with reasonable strength levels to produce alloys targeting high rate performance.

This work demonstrates the interaction of composition and microstructure on the mechanical performance of a medium manganese steel with nominal composition of 0.2C–5Mn–0.25Si–0.2Al–bal. Fe (in wt pct). Various heat treatments are employed to develop different stabilities and quantities of  $\gamma$ -austenite. A pseudo-binary phase diagram, calculated using ThermoCalc 2020b with the TCFE10 database, is shown in Figure 1. In addition to the desired two-phase  $\gamma$ -austenite +  $\alpha$ -ferrite field,  $\theta$ -cementite is stabilized at lower temperatures and higher C concentrations. This work will attempt to elucidate the effect of fluctuations in the nano-scale composition of the phases to better define the mechanical response of the material with greater fidelity than previously reported.

## II. EXPERIMENTAL PROCEDURE

The alloy under investigation was vacuum induction melted and cast into a 14.5 (width)  $\times$  36.0 (length)  $\times$  5.0 (thickness)  $\text{cm}^3$ , 25 kg ingot. The composition of the alloy was 0.21C–5.15Mn–0.24Si–0.21Al–bal. Fe (in wt pct). Chemical analysis was obtained on the cast material by inductively coupled plasma spectrometry after sample dissolution in hydrochloric and nitric acid. Carbon, sulfur, nitrogen and oxygen content were determined using gas combustion analysis. N and S were both  $< 0.005$  wt pct, and oxygen was less than 0.001 wt pct. Hot rolling was performed after heating to  $1150\text{ }^\circ\text{C}$  and holding for two hours after the ingot surface reached the target temperature according to secondary thermocouples placed in direct contact with the sample. Hot rolling was performed within one heating cycle, and the ingot temperature was monitored using an optical pyrometer with an emissivity of 0.92 ( $\varepsilon$

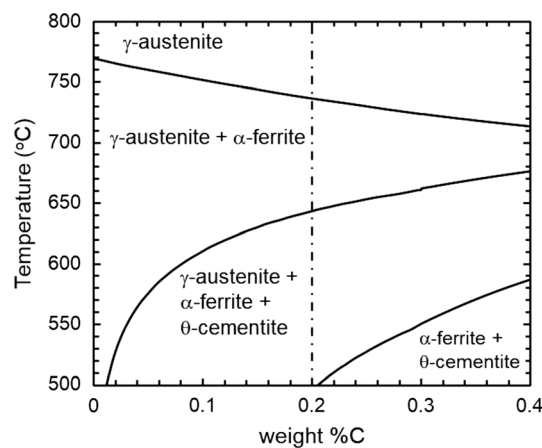


Fig. 1—Pseudo-binary phase diagram of a 5Mn–0.25Si–0.2Al–bal. Fe (in wt pct) alloy showing the effect of carbon on  $\gamma$ -austenite and  $\theta$ -cementite stability.

= 0.92). Hot rolling was completed once the plate reached a gauge thickness of  $12.5 \pm 4$  mm; the plate exit temperature was measured to be  $800 \pm 30$  °C and a total hot reduction of ~ 75 pct was obtained. Upon termination of hot rolling, the plate was immediately transferred to a furnace at 700 °C and held at temperature for one hour followed by air cooling to room temperature. Heat treatment coupons were placed in chemically treated 321 stainless steel bags for oxidation protection. Intercritical annealing heat treatments were performed at 550 °C, 600 °C, and 650 °C for times of 1 to 20 hours. A schematic of the temperatures, strains per pass during hot rolling, and the post-rolling heat treatment is shown in Figure 2.

The phase content was measured through X-ray diffraction using a Bruker D2 Phaser diffractometer with a cobalt radiation source operating at a voltage of 30 kV and current of 10 mA. Scans were carried out with a  $2\theta$  of 45 to 105 deg, a 0.02 deg step size, and integrating for 1 second per step. Phase quantification was performed using Rietveld refinement through the TOPAS™ software. The microstructural disposition of  $\alpha$ -ferrite and  $\gamma$ -austenite was obtained through electron backscattered diffraction using orientation image mapping (EBSD-OIM) as well as phase mapping of the microstructures. Specimens for EBSD-OIM were mechanically polished with a final stage using 0.02  $\mu\text{m}$  colloidal silica solution in a vibratory polisher. Polished specimens were examined in the longitudinal-short plane (perpendicular to both the rolling plane normal and the rolling direction). Orientation image mapping *via* pattern analysis was performed on a ThermoFisher Apreo S using an EDAX Velocity detector. EBSD scans were performed at an accelerating voltage of 20 kV and a working distance of approximately 12 mm. Measurements were performed with a scan step size of 40 nm on a hexagonal grid. Orientation maps were collected for the as-rolled, ICA, and mechanically tested materials. The resulting EBSD maps were analyzed using the MTEX package in Matlab. To observe the deformation behavior of the  $\alpha$ -martensite, the geometrically

necessary dislocation (GND) density was calculated in MTEX. First a half quadratic filter is applied to smooth and reconstruct non-indexed pixels while preserving sub grain boundaries as described by Berhmann *et al.*<sup>[26]</sup> The GND was then determined following the method developed by Pantleon.<sup>[27]</sup>

The scanning transmission electron microscopy (STEM) and precession electron diffraction (PED) were performed using a JEOL 2100F microscope operated at 200 kV. Individual TEM foils were lifted-out and thinned using a ThermoFisher Scientific Helios G4 dual beam microscope with the final thinning occurring at 5 kV to remove/minimize beam damage incurred in earlier thinning steps. The PED was conducted using the NanoMEGAS ASTAR™ platform to generate the nanoscale phase maps for both the 600 °C and 650 °C specimens. PED scans were collected with the electron beam precessed at 0.4 deg and at a scanning step size of 5 nm for the 600 °C specimen and 10 nm for the 650 °C, respectively.

Atom probe tomography (APT) analysis was performed utilizing a Cameca Local Electrode Atom Probe (LEAP) 5000XR system. Atom probe specimens were prepared using an *in situ* lift-out method then annularly ion milled at 5 kV for the final step to minimize Ga implantation with a ThermoFisher Scientific Helios G4 dual beam microscope. APT specimens were run in laser mode with the auto pulse rate control enabled with a minimum mass spectrum range (m/q) of 300 Daltons, pulse energy of 40 pJ, and a target evaporation rate of 0.75 pct, while maintaining at a base temperature of 50 K. A minimum of 25 million ions were collected for each tip analyzed, and a minimum of two tips were analyzed for each condition. The collected datasets were reconstructed using Cameca's Imago Visualization and Analysis Software (IVAS) version 3.8.4 software.

Sub-sized flat ASTM E8<sup>[28]</sup> tensile bars with gauge length of 25 mm and gauge width of 6 mm were electro-discharge machined (EDM) parallel to the rolling direction and tested to understand the effect of heat treatment and austenite content on the tensile behavior of the alloy. Strain was measured using digital image correlation (DIC), and tests were performed in displacement control at a rate of 0.01 mm/s using a 250 kN load cell on an Instron model 5989 frame.

The toughness of the alloy was determined through Charpy V-notch (CVN) impact testing using standard full-sized V-notch samples according to ASTM E23<sup>[29]</sup> at room temperature, nominally 20 °C, - 40 °C, and - 80 °C. The CVN bars were oriented in the T-L direction such that the principal stress was normal to the rolling direction.

### III. RESULTS

The initial microstructure of the alloy in the as-rolled condition is a fully  $\alpha$ -martensitic structure and is shown in Figure 3, this was also confirmed with XRD. The  $\gamma$ -austenite wt fraction as a function of heat treatment time and temperature is shown in Figure 4. It should be noted that the alloy does not contain the calculated

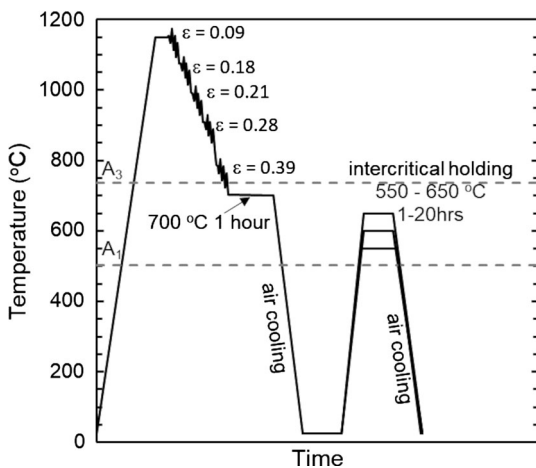


Fig. 2—Schematic of the hot-rolling and heat treatment processing of the alloy under investigation. For reference, the calculated  $A_1$  and  $A_3$  are included.

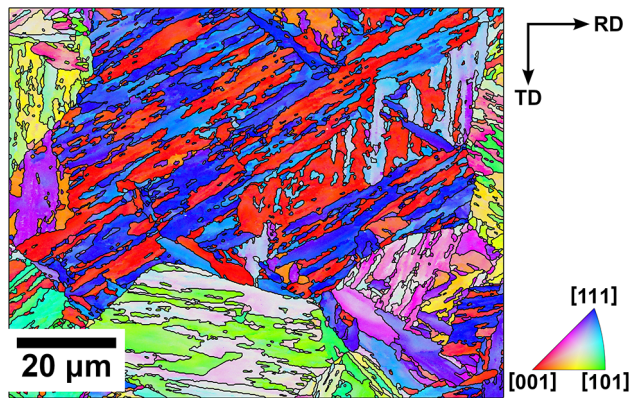


Fig. 3—EBSD-OIM of the as-rolled steel showing a fully martensitic microstructure.

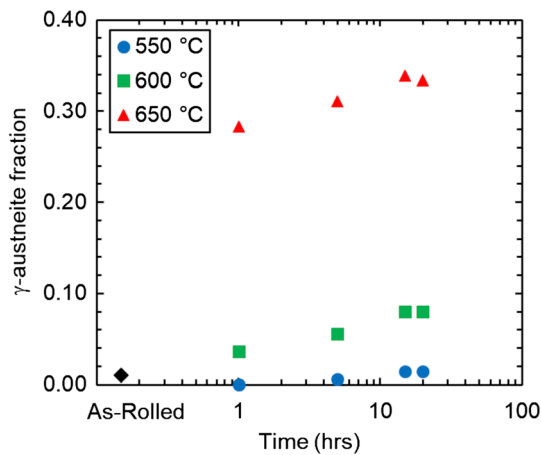


Fig. 4— $\gamma$ -austenite content as measured using XRD as a function of ICA time and temperature.

equilibrium concentration of  $\gamma$ -austenite at any of the heat treatment temperatures. The ThermoCalc calculated  $\gamma$ -austenite wt fractions are 0.05, 0.26, and 0.45 for the 550 °C, 600 °C, and 650 °C intercritical annealing temperatures, respectively. The 600 °C and 650 °C heat treatments will be the focus of this work due to the increased volume of measured  $\gamma$ -austenite, to understand the effect of  $\gamma$ -austenite stability on strength, work hardening, and impact resistance.

EBSD phase maps are shown in Figure 5 for all of the heat treatment times and temperatures. The morphology of the precipitated  $\gamma$ -austenite appears to be interlamellar after annealing treatments performed at 650 °C. Material annealed at 550 °C and 600 °C exhibit fine particles of grain boundary  $\gamma$ -austenite. Based on the measured  $\gamma$ -austenite fractions determined from XRD, the 600 °C and 650 °C samples after annealing for 20 hours were further investigated using quasi-static tensile testing and CVN. An EBSD phase map and the inverse pole figures (IPF) for the  $\gamma$ -austenite and  $\alpha$ -ferrite of the 600 °C—20 hours is shown in Figure 6. It is interesting to note that the  $\gamma$ -austenite consists of globular particles; many of these dispersed particles share a single orientation. The EBSD phase and IPF maps for the  $\gamma$ -austenite and  $\alpha$ -ferrite are shown Figure 7 for the 650 °C—20

hours. The interlamellar  $\gamma$ -austenite is easily identified according to both the phase and OIM map, and the  $\gamma$ -austenite appears to have precipitated and grown between the  $\alpha$ -martensite laths from the as-rolled condition. It is noted that the parent  $\gamma$ -austenite grain is reverted from the child  $\alpha$ -martensite during the ICA treatment, and as with the 600 °C—20 hours sample, local clusters of  $\gamma$ -austenite share a single orientation. This is consistent to what has been observed in high alloy steels as noted by Van Aken *et al.*<sup>[30]</sup> They showed that within either a bainitic or martensitic microstructure, the retained austenite between laths are of the same orientation as the original parent austenite. During re-austenitization, the lenticular islands of austenite grow and impinge upon neighboring austenite of the same orientation and agglomerate into the original parent austenite resulting in no grain refinement from thermal cycling.

Scanning transmission electron microscopy (STEM) was also utilized to identify phases and the sub-micron microstructural features as shown in the bright field images in Figures 8 and 9. It can be seen from Figure 8 that the 600 °C—20 hours condition contained a mixture of  $\alpha$ -ferrite,  $\gamma$ -austenite, and  $\text{Fe}_3\text{C}$ , which is expected from the thermodynamics shown in Figure 1 where the 0.2 wt pct isopleth at 600 °C is in a three-phase regime. It is noted that the carbides are identified as the  $\text{Fe}_3\text{C}$  using select area diffraction (SAD) and form within the  $\alpha$ -ferrite during heat treatment. Figure 9 shows a duplex microstructure in the 650 °C—20 hours condition consisting of solely  $\alpha$ -ferrite and  $\gamma$ -austenite as would be anticipated according to the equilibrium calculations shown previously.

Atom probe tomography was performed to measure the precise composition of the  $\alpha$ -ferrite and  $\gamma$ -austenite. The numerical values were determined using the Fe iso-concentration surfaces set at 85.35 and 86.1 at. pct for the 600 °C—20 hours specimens and 90.06 and 90.13 at. pct for the 650 °C—20 hours specimens, respectively. This method uses all atoms within the individual tips to determine the compositions of the austenite and ferrite phases since the tips were composed entirely of these two phases. Whereas the 1-dimensional concentration profiles of C and Mn in Figures 10 and 11 are generated from the cylinders present in parts b-d for Figures 10 and 11. Thus, they are a much more local chemistry measurement of just the phase boundaries themselves versus the chemistry of the overall austenite and ferrite phases as a whole as shown in Table I. Consequently, the values for the phases chemistries listed in Table I do not directly correspond to the 1D profiles in Figures 10 and 11. This is analogous to doing a 1D EDS profile across an interface versus an EDS map over the two grains composing the interface. The stacking fault energy (SFE) and  $M_s^\alpha$  temperature are calculated for the  $\gamma$ -austenite according to References 31, 32 and 33 based on the composition measured *via* APT in wt pct. It is noted that the  $M_s^\alpha$  of the 650 °C—20 hours condition is slightly above ambient (34 to 38 °C), however with such a low  $M_s^\alpha$  the driving force for transformation is also very low and it is understood that

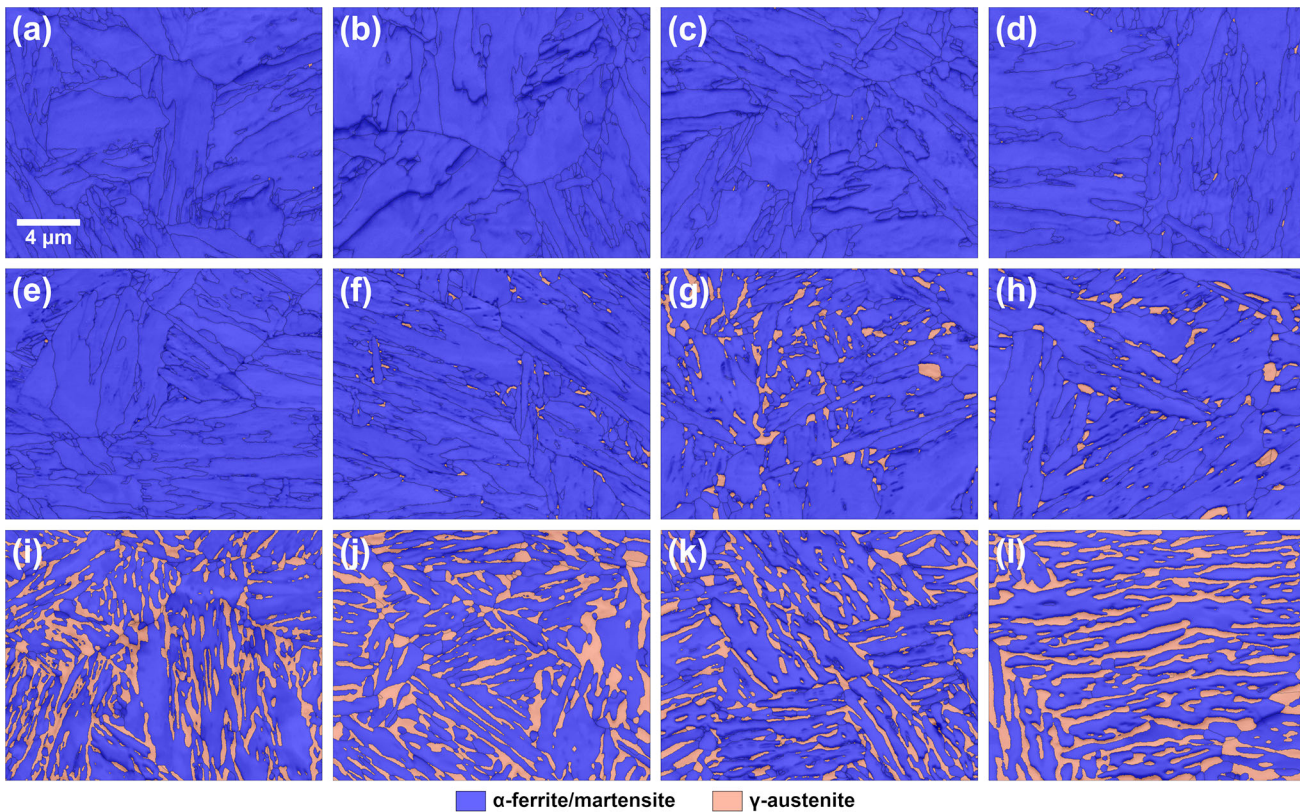


Fig. 5—EBSD phase maps of the alloys intercritically annealed at 550 °C for (a) 1, (b) 5, (c) 15, and (d) 20 h; 600 °C for (e) 1, (f) 5, (g) 15, and (h) 20 hours; and 650 °C for (i) 1, (j) 5, (k) 15, and (l) 20 h. Blue is  $\alpha$ -ferrite/martensite and orange is  $\gamma$ -austenite. All of the phase maps share the same scale (Color figure online).

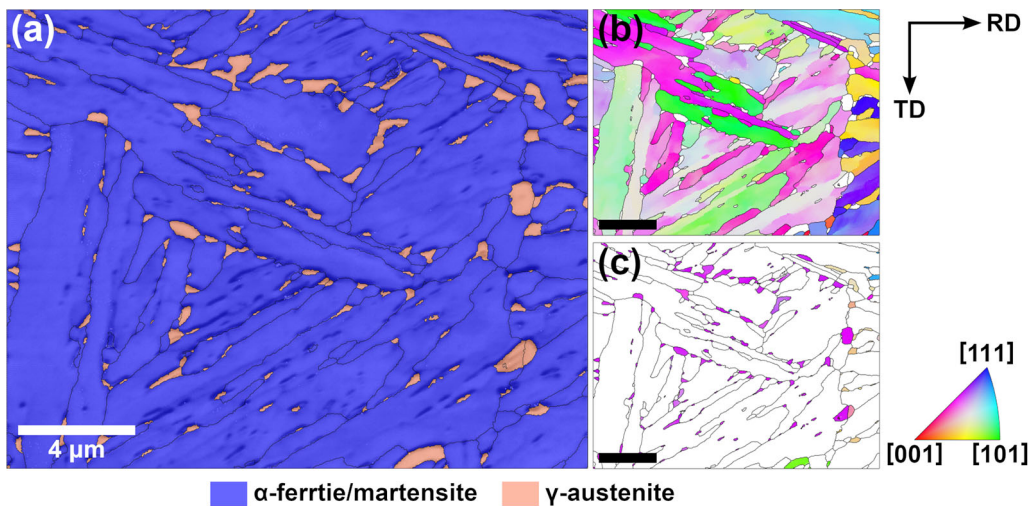


Fig. 6—EBSD phase map (a) of the 600 °C—20 h intercritically annealed condition where blue is  $\alpha$ -ferrite/martensite and orange is  $\gamma$ -austenite. (b) shows the EBSD-OIM of the  $\alpha$ -ferrite/martensite and (c) shows the EBSD-OIM of the  $\gamma$ -austenite. All scale bars are 4  $\mu$ m (Color figure online).

the  $\gamma$ -austenite is sufficiently stable to be retained down to room temperature.

For comparison the equilibrium compositions calculated using ThermoCalc are included in Table II along with their calculated  $M_s^z$  and SFE. It is noted that the  $M_s^z$  of the  $\gamma$ -austenite after processing at 600 °C—20

hours is significantly lower than the 650 °C—20 hours condition, with the calculated  $M_s^z$  as low as  $-181$  °C. This implies that the globular  $\gamma$ -austenite formed during the 600 °C—20 hours heat treatment is significantly more stable than the  $\gamma$ -austenite formed in the 650 °C—20 hours treatment. It is noted that the major

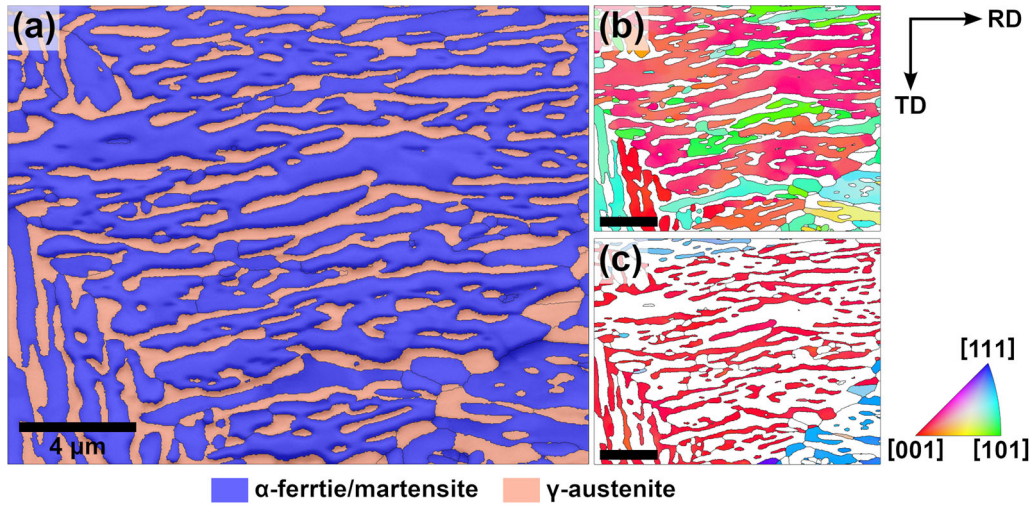


Fig. 7—EBSD phase map (a) of the 650 °C—20 h intercritically annealed condition where blue is  $\alpha$ -ferrite/martensite and orange is  $\gamma$ -austenite. (b) shows the EBSD-OIM of the  $\alpha$ -ferrite/martensite and (c) shows the EBSD-OIM of the  $\gamma$ -austenite. All scale bars are 4  $\mu\text{m}$  (Color figure online).

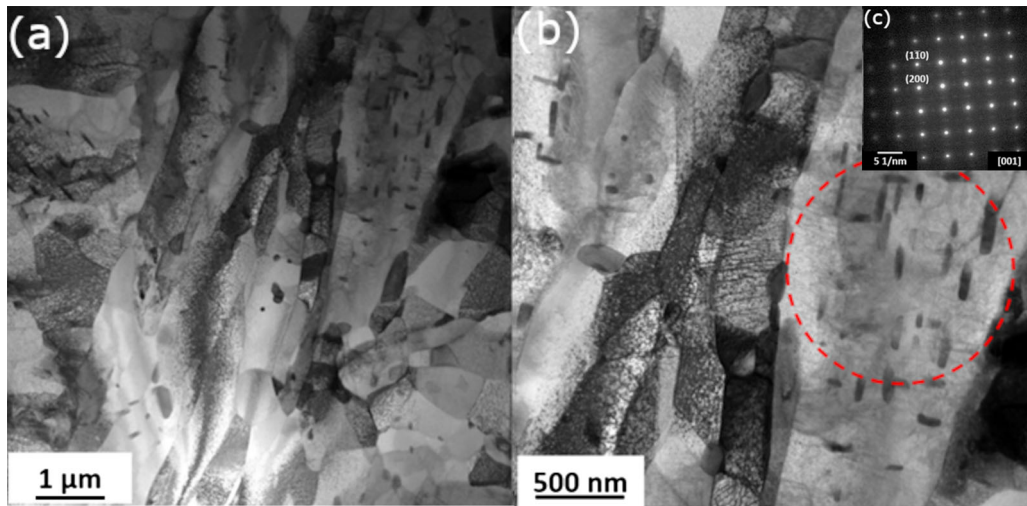


Fig. 8—All images taken from the 600 °C—20 h condition. (a) Low magnification STEM bright field image showing numerous grains and the presence of  $\text{Fe}_3\text{C}$  carbides within certain grains, (b) higher magnification STEM bright field image showing the two variants of  $\text{Fe}_3\text{C}$  being orientated 90 deg to each other (c) additionally the red circle overlaid identifies the area used to generate the selected area diffraction pattern (SAED), finally the SAED indexed as the [001] zone axis of ferrite with additional reflections index as those of  $\text{Fe}_3\text{C}$  (Color figure online).

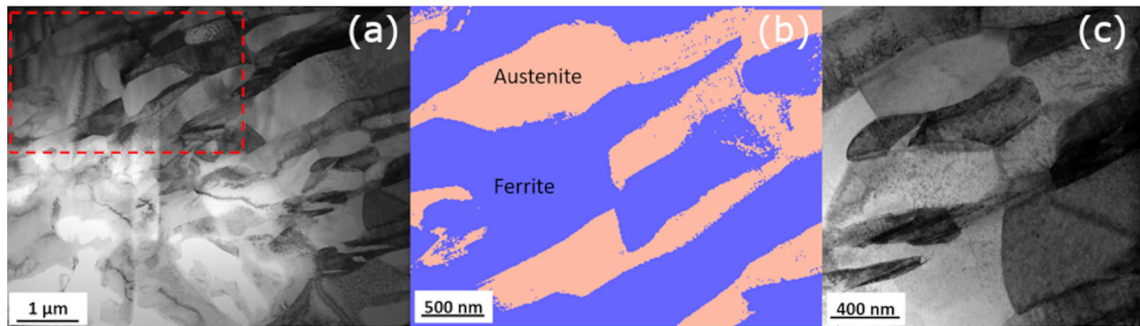


Fig. 9—All images taken from the 650 °C—20 h condition. (a) Low magnification STEM bright field image showing numerous grains as well as overlaid with a red rectangle to identify the area in corresponding phase map, (b) Phase map generated using precession electron diffraction (PED) with the austenite grains shown in orange and the ferrite grains shown in blue, (c) a higher magnification STEM bright field image showing greater detail of the internal grain structure (Color figure online).

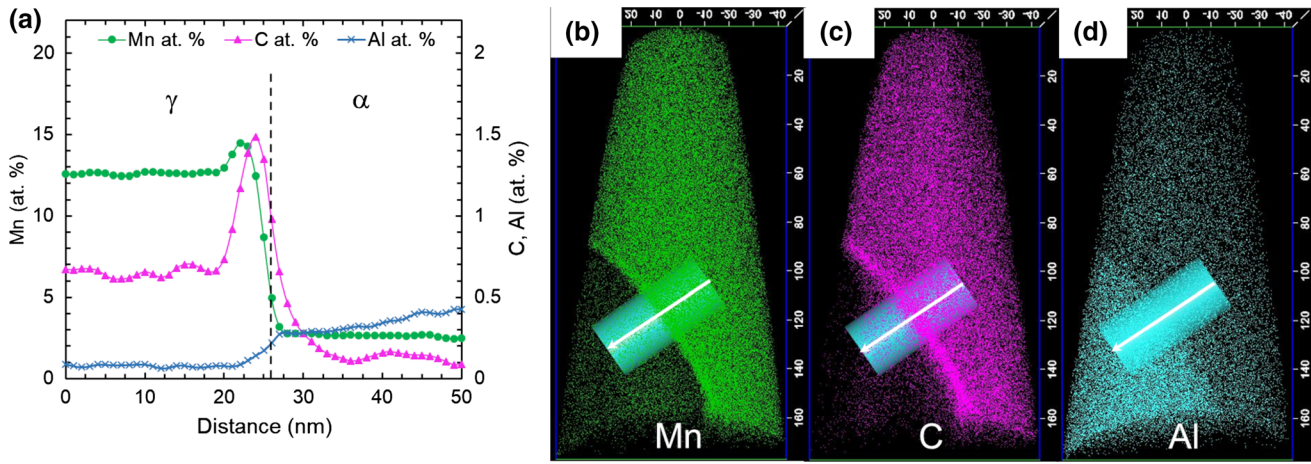


Fig. 10—(a) 1D profile of the 600 °C—20 h intercritically annealed steel. Atom map and isoconcentration surfaces of the full atom probe tip of the (b) manganese, (c) carbon, and (d) aluminum.

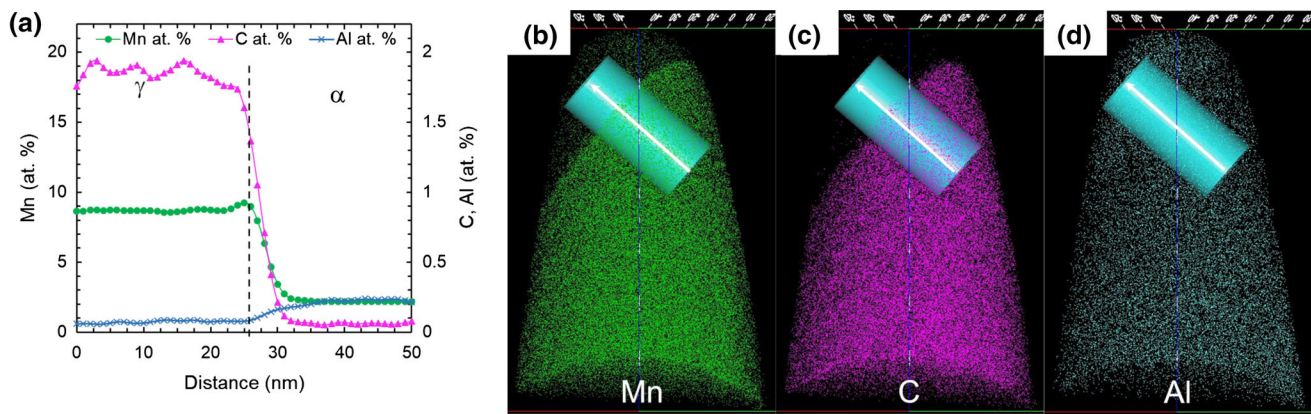


Fig. 11—(a) 1D profile of the 650 °C—20 h condition. Atom map and isoconcentration surfaces of the full atom probe tip of the (b) manganese, (c) carbon, and (d) aluminum.

Table I. Composition of the Analyzed Atom Probe Samples

			C	Mn	Si	Al	Fe	$M_s^\alpha$ °C <sup>[31]</sup>	SFE (mJ/m <sup>2</sup> ) <sup>[32, 33]</sup>
600 °C—T#1	$\gamma$ -austenite	at. pct	1.882	14.138	0.385	0.087	83.508	— 181	2.8
		wt pct	0.413	14.184	0.198	0.043	83.509		
	$\alpha$ -ferrite	at. pct	0.075	2.575	0.535	0.341	96.474	—	—
		wt pct	0.016	2.549	0.270	0.165	97.000		
600 °C—T#2	$\gamma$ -austenite	at. pct	1.758	13.509	0.414	0.059	84.260	— 108	1.8
		wt pct	0.385	13.531	0.212	0.029	85.843		
	$\alpha$ -ferrite	at. pct	0.045	2.875	0.575	0.252	96.253	—	—
		wt pct	0.010	2.843	0.219	0.122	96.806		
650 °C—T#1	$\gamma$ -austenite	at. pct	1.665	9.029	0.421	0.109	88.776	38	4.4
		wt pct	0.364	9.037	0.215	0.054	90.331		
	$\alpha$ -ferrite	at. pct	0.325	4.110	0.471	0.156	94.938	—	—
		wt pct	0.070	4.069	0.238	0.079	95.547		
650 °C—T#2	$\gamma$ -austenite	at. pct	1.780	8.906	0.399	0.094	88.821	34	5.4
		wt pct	0.390	8.921	0.204	0.046	90.439		
	$\alpha$ -ferrite	at. pct	0.159	2.930	0.626	0.117	96.167	—	—
		wt pct	0.159	2.898	0.317	0.057	96.694		

$M_s^\alpha$  and SFE are calculated according to recent work on medium-Mn martensite formation<sup>[31–33]</sup> based on the compositions.

difference in composition between the two heat treatment conditions are the manganese concentrations. The  $\gamma$ -austenite formed after the 600 °C—20 hours heat treatment contains 13.5 to 14 wt pct Mn while the 650 °C—20 hours heat treatment produces a  $\gamma$ -austenite with ~ 9 wt pct Mn.

The representative stress-strain response of the two conditions are shown using both engineering and true behavior in Figure 12. It is noted that the 600 °C—20 hours condition exhibits a higher yield strength and more post-necking ductility. The increased post-necking ductility directly translates to a higher reduction in area and as such greater plasticity. The 650 °C—20 hours condition is significantly different from 600 °C—20 hours condition. The 650 °C—20 hours condition exhibits significant dynamic strain aging, and this leads to a much higher work-hardening rate and ultimate tensile strength. This however comes at a cost and the post-necking ductility is significantly decreased leading to a loss of reduction in area. It is interesting to note that both alloys have comparable total elongations as measured from the tensile test. Yet it can be stated that the 600 °C—20 hours condition produces greater plasticity in the alloy owing to the increased post-necking strain. The strain hardening response was extracted after smoothing the stress-strain curves. First, a 1D Gaussian filter was applied to de-noise the data. For the 650 °C—20 hours sample, which exhibits distinct DSA behavior, the serrations were removed by identifying regions of minimal strain increase. Finally, the hardening data were down sampled by a factor of five and a median filter was applied to smooth any remaining excursions from the average hardening response. The measured values of the quasi-static properties are summarized in Table III.

The CVN impact energy as a function of testing temperature for both the 600 °C—20 hours and 650 °C—20 hours conditions are shown in Figure 13, where the as-rolled properties are also shown as a reference of the fully  $\alpha$ -martensitic structure. The 600 °C—20 hours condition exhibited the highest impact energy at all test temperatures with a room temperature impact energy of  $183 \pm 5$  J and a  $-80$  °C impact energy of  $43 \pm 2$  J. The 650 °C intercritically annealed sample produces a higher impact energy when tested at room temperature as compared to the as-rolled steel ( $94 \pm 3$  J vs.  $50 \pm 9$  J); however upon testing the 650 °C—20 hours condition at  $-80$  °C and  $-40$  °C, the impact values of the 650 °C—20 hours condition do not vary significantly from the as-rolled martensitic steel.

#### IV. DISCUSSION

This investigation focuses on the effect of heat treatment temperature on microstructure and properties. The 600 °C heat treatments produce a more globular, equiaxed  $\gamma$ -austenite. This is in agreement with previous works on medium-Mn steels<sup>[2,18]</sup> which showed that the equiaxed  $\gamma$ -austenite is significantly more stable than the interlamellar  $\gamma$ -austenite as observed in this work after the 650 °C processing. The

root cause for the difference in  $\gamma$ -austenite morphology is not determined in this study and further investigation is forthcoming. The 600 °C—20 hours condition comprises a triplex microstructure of  $\alpha$ -ferrite,  $\gamma$ -austenite, and carbides identified as  $\theta$ -Fe<sub>3</sub>C. This is in agreement with the equilibrium phase diagram shown in Figure 1, though the final phase fractions have not achieved thermodynamic equilibrium even after a 20 hour ICA. According to thermodynamic calculations, the predicted microstructure should comprise 17 wt pct  $\gamma$ -austenite, 80 wt pct  $\alpha$ -ferrite, and 3 wt pct cementite; however only 8 wt pct  $\gamma$ -austenite is observed.

The 650 °C heat treatment produces a higher fraction of  $\gamma$ -austenite as is anticipated from the thermodynamic stability shown in Figure 1, and is supported by the kinetics at which elements can diffuse compared to 600 °C. At 650 °C the alloy is within a dual-phase field of  $\gamma$ -austenite and  $\alpha$ -ferrite, and this is the microstructure revealed through XRD, EBSD, and TEM. The phase fractions are not at the equilibrium quantities with the calculated  $\gamma$ -austenite being 45 wt pct and a measured  $\gamma$ -austenite content of 33 wt pct. A maximum  $\gamma$ -austenite concentration of 35 wt pct is first realized at 15 hours and drops to 33 wt pct as annealing progresses. The higher  $\gamma$ -austenite content translates to a lower enrichment of Mn and presumably C within the  $\gamma$ -austenite as compared to the 600 °C—20 hours condition. As measured using APT the Mn does see a shift in enrichment however the carbon content is only slightly shifted with a difference of 0.03 wt pct as shown in Table I. Even with the similar C concentrations within the  $\gamma$ -austenite, the lowered Mn content causes the calculated  $M_s^\alpha$  temperature to increase relative to the 600 °C—20 hours condition. This was discussed accordingly in the work by Field *et al.*,<sup>[31]</sup> which showed that Mn had a greater influence on the temperature dependent driving force for  $\alpha$ -martensite formation within medium-Mn steels. The carbon content of the  $\alpha$ -ferrite within the 650 °C—20 hours condition is higher as compared to the 600 °C—20 hours condition and is due to the  $\theta$ -carbides formed during the 600 °C intercritical annealing treatment, which are not observed at 650 °C. The  $M_s^\alpha$  of the  $\gamma$ -austenite formed in the 650 °C—20 hours condition is above ambient as presented in Table I. Arlazarov *et al.*<sup>[12]</sup> showed in their work that chemical enrichment was not sufficient to reduce the  $M_s^\alpha$  to below ambient and noted retained  $\gamma$ -austenite contents of 22 vol pct even though the  $M_s^\alpha$  was calculated to be 203 °C.

The phase fractions are not at their respective equilibrium contents due to kinetic constraints. It is interesting to observe that the composition of the phases are also at a metastable state. The average composition of the  $\gamma$ -austenite formed after the 600 °C ICA treatments was 0.40C–13.9Mn–0.21Si–0.04Al–bal.Fe (wt pct) and is significantly richer in C and Mn content compared to the equilibrium composition of 0.33C–13.0Mn–0.36Si–0.05Al–bal.Fe (wt pct). The same effect is noted in the 650 °C ICA condition, where the  $\gamma$ -austenite has a measured composition of 0.46C–9.55Mn–0.22Si–0.05Al–bal.Fe (wt pct), compared to the equilibrium composition of



**Table II. Thermodynamic Equilibrium Composition as Calculated According to ThermoCalc2020b**

			C	Mn	Si	Al	Fe	$M_s^{\alpha} \text{ }^{\circ}\text{C}^{[31]}$	SFE ( $\text{mJ}/\text{m}^2$ ) <sup>[32, 33]</sup>
600 °C	$\gamma$ -austenite	at. pct	1.507	12.946	0.703	0.110	84.735	− 37	0.4
		wt pct	0.330	12.969	0.360	0.054	86.287		
	$\alpha$ -ferrite	at. pct	0.005	2.738	0.461	0.486	96.310	18	7.7
		wt pct	0.001	2.708	0.233	0.236	96.822		
650 °C	$\gamma$ -austenite	at. pct	1.985	8.822	0.553	0.188	88.451	18	7.7
		wt pct	0.436	8.863	0.284	0.093	90.323		
	$\alpha$ -ferrite	at. pct	0.014	2.105	0.439	0.595	96.847	—	—
		wt pct	0.003	2.083	0.222	0.289	97.403		

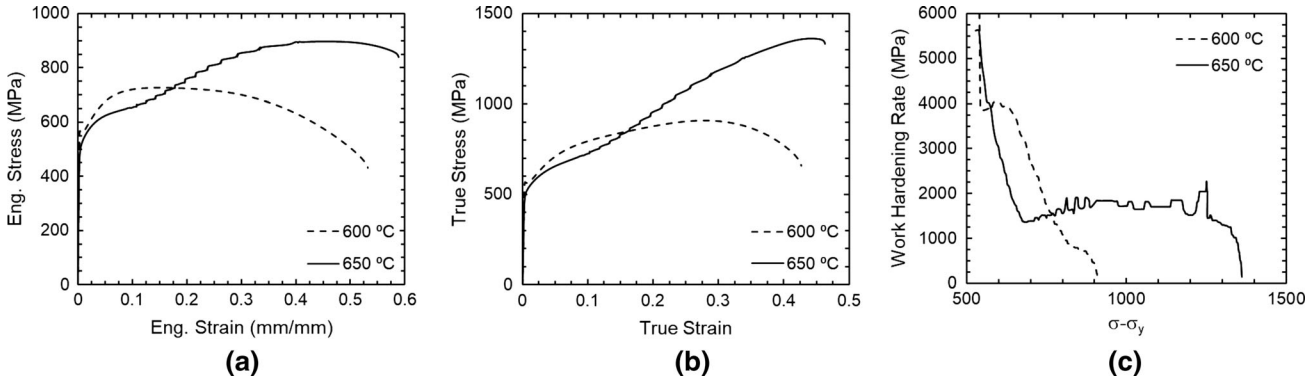


Fig. 12—(a) Engineering, (b) True stress-strain, and (c) work hardening response of the alloy after intercritical heat treatment for 20 h.

**Table III. Quasi-static Tensile Properties of the Intercritically Annealed Alloy**

Heat Treatment	Yield Stress (MPa)	Engineering Peak Stress (MPa)	True Ultimate Stress (MPa)	Eng. Strain (mm/mm)	True Strain	Reduction in Area—True Strain
600 °C	535 ± 17	733 ± 3	910 ± 1	0.52 ± 0.01	0.42 ± 0.01	1.04 ± 0.11
650 °C	494 ± 19	888 ± 3	1350 ± 20	0.57 ± 0.01	0.44 ± 0.01	0.35 ± 0.01

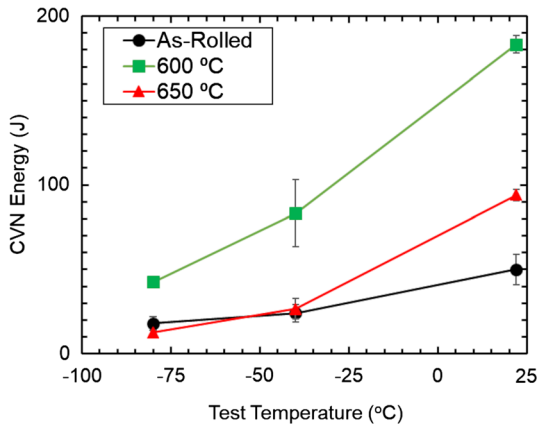


Fig. 13—CVN energy absorption as a function of testing temperature.

0.38C–8.98Mn–0.21Si–0.05Al–bal.Fe (wt pct). The 650 °C ICA however produces  $\gamma$ -austenite closer in composition to the calculated equilibrium values and is due to

the increased mobility of Mn at higher temperatures. It is interesting to note that recent work by Varanasi *et al.*<sup>[34]</sup> showed that pipe diffusion along dislocations can accelerate the formation and stabilization of  $\gamma$ -austenite even when the ICA treatment temperature (500 °C) was low and the anticipated diffusion would be extremely sluggish. However their work focused on cold-worked medium-Mn steel, which would contain significantly higher dislocation densities. Their results are consistent with this work and Varanasi noted that the total quantity of  $\gamma$ -austenite produced during annealing is typically below the equilibrium concentration. This is generally attributed to slow diffusion kinetics of substitutional elements like Mn. As a consequence of the reduced concentration of  $\gamma$ -austenite and to provide a zero net change in the composition, the  $\gamma$ -austenite is enriched in Mn and C according to the mass balance of elements. This would imply that the phase boundary stability is a rate limiting step compared to the elemental mobility, which is assisted by diffusion short circuits like grain boundaries and dislocations. The phase boundary mobility also translates to a change

**Table IV. Evolution of the  $\gamma$ -Austenite Percentage as a Function of Test Conditions**

Heat Treatment	Initial (wt pct $\gamma$ )	After Quasi-static Fracture	After CVN Fracture	Cooled to $-40$ °C	After $-40$ °C CVN Fracture
600 °C	8	0	7	8	6
650 °C	33	0	15	20	10

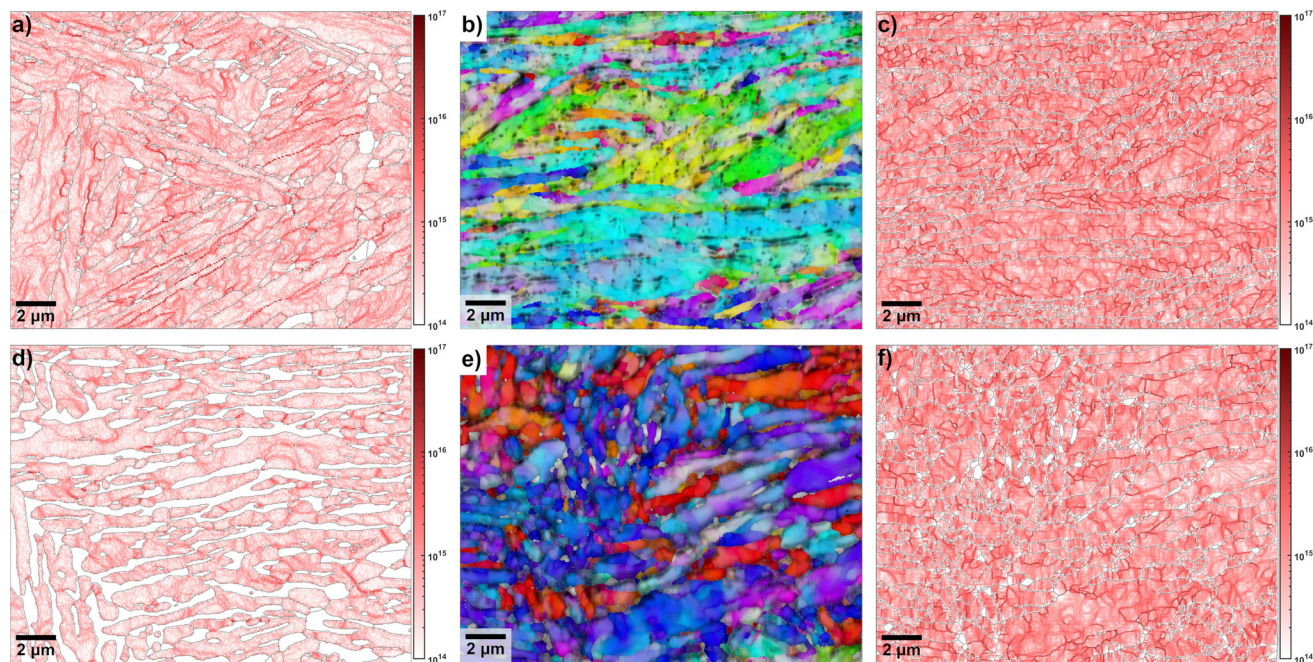


Fig. 14—(a) GND map of the as-heat-treated, (b) tensile deformed to failure IPF, and (c) GND map of the tensile deformed 600 °C—20 h specimen. (d) GND map of the as-heat-treated, (e) tensile deformed to failure IPF, and (f) GND map of the tensile deformed 650 °C—20 h specimen.

in the morphology of the precipitated  $\gamma$ -austenite. As is shown in Figure 5 the  $\gamma$ -austenite formed during the 650 °C heat treatments is more lenticular and growth is assumed to have proceeded along prior martensite laths leading to the lamellar-like structure presented in this work in Figures 5, 6 and 7. The 600 °C heat treatment produces a more equiaxed  $\gamma$ -austenite structure and this implies that the phase boundary was less mobile and growth was controlled by the diffusion of elements (*e.g.* C and Mn) along grain boundaries. This is also corroborated with the local enrichment of Mn and C at the grain boundary as shown in Figure 10 of the 1D atomic profile for the 600 °C—20 hours condition.

The mechanical behavior of the two ICA treatments are significantly different. The lower temperature annealed steel exhibits a slightly higher yield strength, very high post-necking ductility, and significantly improved CVN toughness. Conversely, the 650 °C—20 hours condition exhibits significantly higher work hardening rates leading to nearly a 50 pct increase in the true ultimate strength (910 to 1350 MPa) without a

significant loss in total elongation. However, these properties come at a cost to the post-necking ductility, reduction in area, and Charpy V-notch toughness.

To understand the cause of this effect the microstructure was interrogated and is shown in Figures 8 and 9. Figure 8 indicates the 600 °C—20 hours sample contains a triplex microstructure of  $\alpha$ -ferrite,  $\gamma$ -austenite, and a small fraction of  $\theta$ -carbide. It is postulated that the  $\theta$ -carbide acts as a strengthening mechanism to the 600 °C—20 hours treated specimens to a greater degree than the solid solution strengthening effect of C in the  $\alpha$ -ferrite. The 650 °C—20 hours condition has a higher C content in the  $\alpha$  phase ( $0.06 \pm 0.015$  vs  $0.24 \pm 0.08$  at. pct C) compared to the 600 °C—20 hours condition; with similar equivalent C contents in the  $\gamma$ -austenite ( $0.40 \pm 0.02$  vs  $0.38 \pm 0.02$  wt pct C) for both conditions. The formation of the  $\theta$ -carbide provides a strengthening effect as would be anticipated within traditional steels. It is also understood that the  $\theta$ -carbide is a hard dislocation barrier as stated in the literature.<sup>[35]</sup> In addition, significant dynamic strain aging during quasi-static tension testing is observed for the 650 °C—20 hours condition in Figure 12. It has been well

documented that DSA is closely associated with an increase in work hardening rate and negative strain rate sensitivity.<sup>[15,32,36]</sup> The reduction in post-necking ductility can also be related to DSA where the local strain rate at the formation of the initial plastic instability within the necked region leads to reduced post-necking strain prior to failure.<sup>[33]</sup> DSA behavior of the steel also occurs in conjunction with the absence of  $\theta$ -carbide; the 650 °C—20 hours condition was found to be lacking in carbides and as such had a higher carbon concentration within the  $\alpha$ -ferrite as noted previously. This is in close agreement with the work by Field and Van Aken,<sup>[15]</sup> who showed that DSA in a dual-phase 10 wt pct Mn TRIP steel was associated with C and N diffusion in the  $\alpha$ -ferrite. They also showed that by proper alloying the DSA effect could be mitigated by alloying to produce carbides and tie up solid solution C either in the  $\alpha$ -ferrite or  $\gamma$ -austenite. That work calculated the activation energy for DSA and found that when carbides were present the activation energy for DSA was comparable to Mn diffusion in steel.

One might postulate that the serrations observed in the 650 °C—20 hours condition are correlated with the stress-assisted transformation of the  $\gamma$ -austenite during testing, while the 600 °C—20 hours condition does not produce a TRIP effect during quasi-static testing but this is not the case. To determine this, XRD of the post-mortem tensile bars was performed near the fracture surface, as is shown in Table IV. The measured  $\gamma$ -austenite content near the neck for both the 650 °C—20 hours and 600 °C—20 hours conditions are below the measurement threshold according to X-ray diffraction, indicating that during the quasi-static tension testing of this alloy the  $\gamma$ -austenite will transform. This is also corroborated by the work-hardening behavior as shown in Figure 12(c). The 650 °C—20 hours condition exhibits a diffuse, but increasing instantaneous work hardening rate till a maximum is obtained as has been reported for TRIP steels.<sup>[25]</sup> The 600 °C—20 hours condition exhibits a similar behavior however the stress level at which the peak rate occurs is severely truncated. This also is noted from the stress-strain curve that the max stress, and uniform elongation are much lower than the 650 °C—20 hours condition; however it is still evident from the XRD and the work-hardening behavior that the 600 °C—20 hours treated steel exhibits the TRIP character during quasi-static tensile deformation.

While the  $\gamma$ -austenite behavior is a significant topic of research in this class of steel, understanding the effect of  $\alpha$ -ferrite on deformation behavior should not be dismissed. To understand the effect of  $\alpha$ -ferrite on the deformation structure the GND density was calculated and mapped for the as-heat-treated material and the tensile test samples as shown in Figure 14. Here, the as-heat treated EBSD maps [Figure 14(a) & (d)] correspond to Figure 6(b) and Figure 7(b) for the 600 °C 650 °C ICA samples, respectively. It can be seen that the  $\alpha$ -ferrite deforms from slip and through the imposition of a strain the GND density increases significantly between the pre and post tested conditions. It is interesting to note that in the initial as-heat treated

state the GNDs appear to align according to sub-boundaries according to the incoming  $\alpha$ -martensitic structure from the as-rolled condition. This indicates that through the intercritical annealing process at either 600 °C or 650 °C the  $\alpha$ -martensite is tempered to become a heavily tempered  $\alpha$ -martensitic structure. Following deformation, the overall dislocation density is significantly increased and additional subgrain boundaries are formed within the  $\alpha$ -martensite laths, indicative of dislocation mediated plasticity.

The effect of  $\gamma$ -austenite has a significantly different impact on the CVN toughness than the quasi-static mechanical response. The 650 °C—20 hours condition appears to contain the best properties as measured according to the quasi-static results with a product of ultimate stress and total elongation of 50.6 GPa·pct compared to the 600 °C—20 hours condition that produces a product of ultimate stress and total elongation of 38.1 GPa·pct. However as observed in Figure 13, the 650 °C—20 hours showed a reduction in CVN toughness values (83 J to 27 J at  $-40^{\circ}\text{C}$ ) and were comparable to the as-rolled fully martensitic condition. Additional XRD and EBSD investigations were

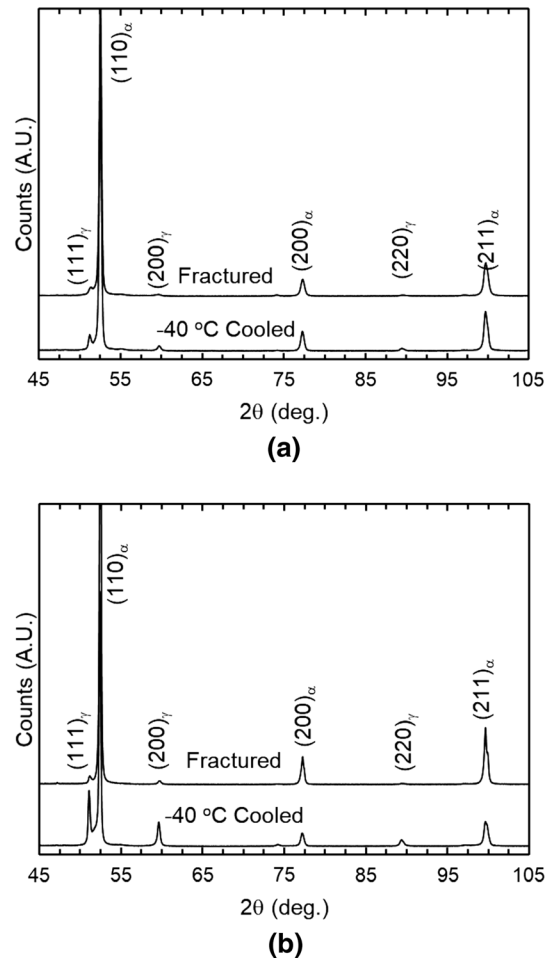


Fig. 15—X-ray diffraction spectra of the steel after cooling the alloy down to  $-40^{\circ}\text{C}$  and as well as the fracture surface after CVN testing at  $-40^{\circ}\text{C}$  of the (a) 600 °C—20 h and (b) 650 °C—20 h conditions.

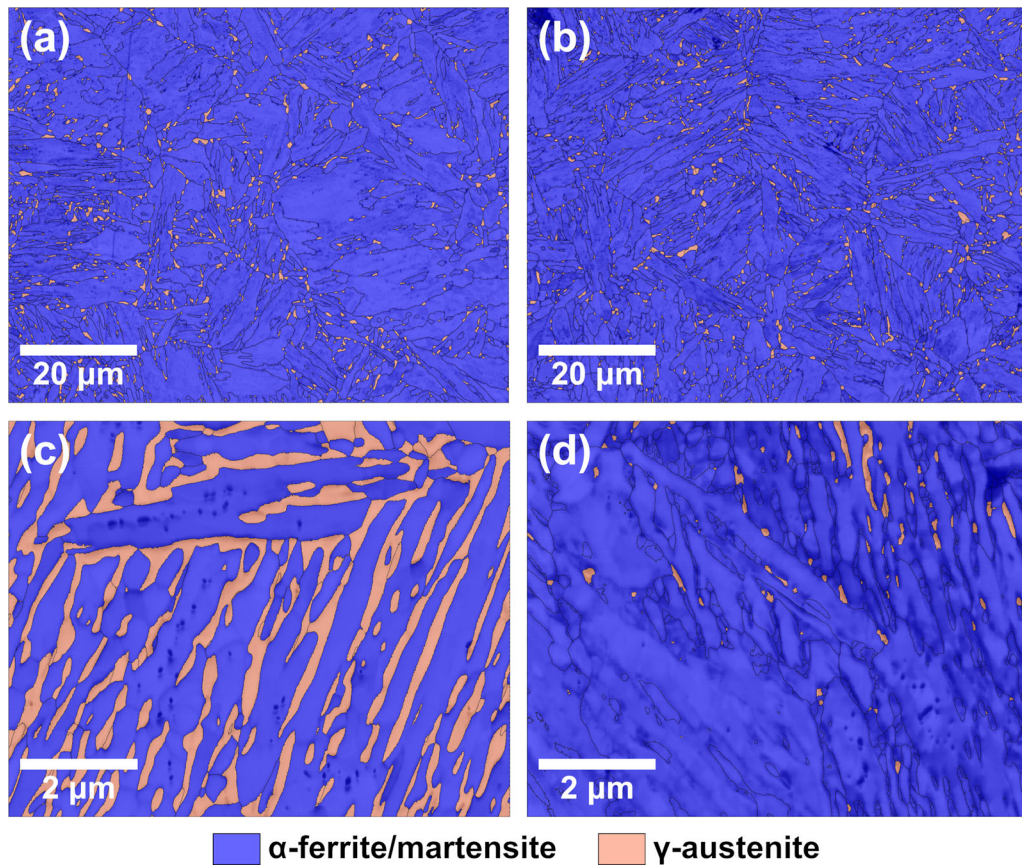


Fig. 16—EBSD-Phase map of 600 °C (a) cooled to -40 °C, and (b) cooled to -40 °C and Charpy impact tested, and 650 °C (c) cooled to -40 °C, and (d) cooled to -40 °C and CVN tested, note Figures (a) and (b) are a different scale than Figures (c) and (d).

performed to determine the state of the  $\gamma$ -austenite after cooling to the test temperature as well as after testing at -40 °C for both the 600 °C—20 hours and 650 °C—20 hours conditions. From the XRD spectra shown in Figure 15, as well as the calculated concentration of  $\gamma$ -austenite, the stability of the  $\gamma$ -austenite within the 650 °C—20 hours intercritically annealed steel is less than the  $\gamma$ -austenite precipitated after 600 °C—20 hours intercritical annealing treatment. This is also supported by what is shown in Table I that the  $M_s^z$  of the 650 °C—20 hours  $\gamma$ -austenite is as low as 36 °C, which is greater than the testing temperature of -40 °C. The work by Holloman and Jaffe<sup>[24]</sup> stated that if the  $\gamma$ -austenite is not sufficiently stable the fresh  $\alpha$ -martensite will act as a cleavage crack initiation site, reducing the fracture strength of the alloy. Niikura and Morris<sup>[18]</sup> noted on their study of high toughness 5Mn steels that a loss in toughness was due to the intrusion of  $\epsilon$ -martensite during impact testing. From the EBSD phase maps shown in Figure 16, there was no discernable  $\epsilon$ -martensite. It can be seen that the optimum microstructure for both strength and toughness is best obtained by not just maximizing the quantity of the  $\gamma$ -austenite. The stability of the  $\gamma$ -austenite must be accounted for, especially where low temperature, *i.e.* -40 °C Charpy toughness is required. The lower temperature 600 °C—20 hours ICA provided lower  $\gamma$ -austenite concentration; however,

the synergy of reduced  $\gamma$ -austenite as well as the precipitation of  $\theta$ -carbide produced  $\gamma$ -austenite that was sufficiently stabilized to below -40 °C, while yield strength was improved through carbide strengthening. The  $\alpha$ -ferrite dislocation structure is also considered, as shown in Figure 14, and it can be seen that from intercritical annealing the recovery of the transformation induced dislocations which are noted in the as-rolled state are reoriented into a subgrain structure as noted previously. The subgrain structures for both heat treatment conditions are very similar and it would imply that the change in toughness is primarily due to the stability of  $\gamma$ -austenite as modified by heat treatment, where the  $\gamma$ -austenite athermally transforms upon cooling to fresh brittle  $\alpha$ -martensite upon cooling to the test temperature, producing a mixed microstructure of untempered  $\alpha$ -martensite, with a carbon content of ~0.38 wt pct (see Table I), and  $\alpha$ -ferrite.

## V. CONCLUSION

In this work, a hot-rolled medium-Mn steel was intercritically annealed at temperatures ranging from 550 °C to 650 °C and times ranging from 1 to 20 hours to reveal the correlation between microstructural properties, *e.g.*, phase fraction and local composition of

phases, with mechanical properties, *e.g.*, the uniaxial tensile behavior and fracture resistance. Higher annealing temperatures and longer times produced a microstructure with increasing  $\gamma$ -austenite fraction that approached but did not reach the theoretical equilibrium concentration of  $\gamma$ -austenite or elemental concentration within the  $\gamma$ -austenite phase. While it may be hypothesized that the material with a greatest fraction of  $\gamma$ -austenite (33 pct for ICA at 650 °C—20 hours condition compared with 8 pct for ICA at 600 °C—20 hours condition) would yield improved fracture properties—this was not the case. Instead, the material that was intercritically annealed at 600 °C with only 8 pct fraction of  $\gamma$ -austenite had significantly improved CVN toughness compared with the 650 °C—20 hours, despite its higher initial yield strength. This indicates that the quantity of the  $\gamma$ -austenite alone does not correlate well with the measured properties.

Atom Probe Tomography was used to reveal the difference in composition between the  $\gamma$ -austenite for the 600 °C and 650 °C samples. It was found that in the 650 °C—20 hours condition a large fraction of  $\gamma$ -austenite starves the material of  $\gamma$ -stabilizing elements within the  $\gamma$ -austenite, which is reflected in a higher calculated  $M_s^z$  temperature and lower austenite stability. On the other hand, the  $\gamma$ -austenite in the 600 °C—20 hours condition is enriched with  $\gamma$ -stabilizing elements due its low concentration. Despite the presence of  $\theta$ -Fe<sub>3</sub>C carbides in the 600 °C—20 hours condition, which reduces the carbon content that would otherwise stabilize the austenite matrix, the  $\gamma$ -austenite possesses a lower calculated  $M_s^z$  temperature that indicates greater austenite stability. Increased austenite stability correlates directly with the improvement in CVN toughness from room temperature down to – 80 °C. Observation of CVN samples before and after testing revealed that at low temperatures the formation of fresh  $\alpha$ -martensite likely undermines the fracture toughness in the 650 °C—20 hours condition due to the low  $\gamma$ -austenite stability compared with the 600 °C—20 hours condition. It is also noted that the presence of  $\theta$ -Fe<sub>3</sub>C carbides in the 600 °C—20 hours condition prevents DSA, which is observed under room temperature tension tests in the 650 °C—20 hours condition. This work shows that austenite stability and the relative partitioning of elements between phases provides significantly greater insight into the observed mechanical and fracture behavior than concentration of individual phases alone.

#### ACKNOWLEDGMENTS

The authors acknowledge the support of Dr. Timothy Walter in performing the tension tests and DIC data analysis, in particular Mr. Franklin Kellogg's assistance in operating the X-ray diffractometer was instrumental to this work.

#### CONFLICT OF INTEREST

The authors declare that they have no conflict of interest.

#### REFERENCES

1. R.L. Miller: *Met. Trans. B.*, 1972, vol. 3, pp. 905–12.
2. M.J. Merwin: *Mater. Sci. Forum.*, 2007, vol. 539–543, pp. 4327–32.
3. H. Huang, O. Matsumura, and T. Furukawa: *Mater. Sci. Technol.*, 1994, vol. 10, pp. 621–26.
4. D.E. Kim, Y.K. Park, O.Y. Lee, K.G. Jin, et al.: *Korean. J. Mater. Res.*, 2005, vol. 15, pp. 115–23.
5. J. Shi, X. Sun, M. Wang, W. Hui, H. Dong, and W. Cao: *Scr. Mater.*, 2010, vol. 63, pp. 815–18.
6. H. Luo, H. Dong, and M. Huang: *Mater. Des.*, 2015, vol. 83, pp. 42–8.
7. S. Lee, S.-J. Lee, S. Santhosh Kumar, K. Lee, and B.C. De Cooman: *Met. Trans. A*, 2011, vol. 42A, pp. 3638–51.
8. Y. Zhang, L. Wang, K.O. Findley, and J. Speer: *Met. Trans. A.*, 2017, vol. 48A, pp. 2140–49.
9. J. Han, S.-H. Kang, S.-J. Lee, and Y.-K. Lee: *J. Alloy Compd.*, 2016, vol. 681, pp. 580–88.
10. J. Han, S.-J. Lee, J.-G. Jung, and Y.-K. Lee: *Acta Mater.*, 2014, vol. 78, pp. 369–77.
11. P.J. Gibbs, E. De Moor, M.J. Merwin, B. Clausen, J.G. Speer, and D.K. Matlock: *Met. Trans. A.*, 2011, vol. 42A, pp. 3691–701.
12. A. Arlazarov, M. Goune, O. Bouaziz, A. Hazotte, G. Petigand, and P. Barges: *Mater. Sci. Eng. A.*, 2012, vol. 545, pp. 31–39.
13. D.M. Field and D.C. Van Aken: *Met. Trans. A.*, 2016, vol. 47A, pp. 1912–17.
14. D.M. Field, J. Qing, and D.C. Van Aken: *Met. Trans. A.*, 2018, vol. 49, pp. 4615–32.
15. D.M. Field and D.C. Van Aken: *Met. Trans. A.*, 2018, vol. 49(4), pp. 1152–66.
16. D.J. Magagnosc, D.M. Field, C.S. Meredith, T.R. Walter, K.R. Limmer: *J.T. Lloyd, Mater. Sci. Eng. A*, 2020, 799, <https://doi.org/10.1016/j.msea.2020.140252>.
17. Z.Z. Zhao, J.H. Liang, A.M. Zhao, J.T. Liang, D. Tang, and Y.P. Gao: *J. Alloy Compd.*, 2017, vol. 691, pp. 51–59.
18. M. Niikura and J.W. Morris: *Met Trans. A.*, 1980, vol. 11, pp. 1531–40.
19. J. Hu, L.-X. Du, W. Xu, J.-H. Zhai, Y. Dong, Y.-J. Liu, and R.D.K. Misra: *Mater. Charact.*, 2018, vol. 136, pp. 20–28.
20. J.I. Kim, C.K. Syn, and J.W. Morris: *Metall. Trans. A.*, 1983, vol. 14, pp. 93–103.
21. D.M. Field, J.S. Montgomery, K.R. Limmer, and K. Cho: *Met. Trans. A.*, 2020, vol. 51, pp. 1038–43.
22. D.M. Field, S.R. Cluff, K.R. Limmer, J.S. Montgomery, K.C. Cho: *Metals*, vol. 11(5), p. 723. <https://doi.org/10.3390/met11050723>.
23. J. Chen, C. Li, J. Ren, X. Tu, and L. Chen: *Mater. Sci. Eng. A.*, 2019, vol. 754, pp. 178–89.
24. J.H. Holloman and L.D. Jaffe, WAL 320/28 (ADa951095): *The Metallurgical Design of Steels for Optimum Mechanical Properties*, Watertown Arsenal Laboratories, 1945.
25. D.M. Field, L.G. Garza-Martinez, and D.C. Van Aken: *Met. Trans. A.*, 2020, vol. 51, pp. 4427–33.
26. R. Bergmann, R. Chan, R. Hielscher, J. Persch, and G. Steidl: *Inverse Probl. Imaging.*, 2016, vol. 10, pp. 281–304.
27. W. Pantleon: *Scr. Mater.*, 2008, vol. 58, pp. 994–97.
28. ASTM STandard E8-16a: ASTM International, West Conshohocken PA, 2016 [https://doi.org/10.1520/e0008\\_e0008m-16a](https://doi.org/10.1520/e0008_e0008m-16a).
29. ASTM STandard E23-18: ASTM International, West Conshohocken PA, 2018 <https://doi.org/10.1520/e0023-18>.
30. D.C. Van Aken, T.O. Webb, and J.D. Green: *23rd International Federation of Heat Treatment and Surface Engineering Congress*, Savannah GA, 2016, pp. 262–72.

31. D.M. Field, D.S. Baker, and D.C. Van Aken: *Met. Trans. A.*, 2017, vol. 48, pp. 2150–63.
32. S.T. Pisarik and D.C. Van Aken: *Met. Trans. A.*, 2016, vol. 47, pp. 1009–18.
33. J.T. Lloyd, D.M. Field, and K.R. Limmer: *Mater. Des.*, 2020, <https://doi.org/10.1016/j.matdes.2020.108878>.
34. R.S. Varanasi, M. Lipinska-Chwatek, J. Mayer, B. Gault, and D. Ponge: *Scr. Mater.*, 2022, <https://doi.org/10.1016/j.scriptamat.2021.114228>.
35. B.C. De Cooman and J.G. Speer: “Austenite Decomposition in Fe-C-X Alloy Systems,” *Fundamentals of Steel Product Physical Metallurgy*, 1st Edition, ASM International, Materials Park, OH, 2011, p. 77.
36. P. Rodriguez: *Bull. Mater. Sci.*, 1984, vol. 6, pp. 653–63.

**Publisher’s Note** Springer Nature remains neutral with regard to jurisdictional claims in published maps and institutional affiliations.